

3D mesoporous silica networks with improved diffusion and interference-abating properties for electrochemical sensing

Luca Rimoldi^{a,b,*}, Valentina Pifferi^{a,b,*}, Daniela Meroni^{a,b,*}, Guido Soliveri^c, Silvia Ardizzone^{a,b},
Luigi Falciola^{a,b}

^a *Dipartimento di Chimica, Università degli Studi di Milano, Via Golgi 19, 20133 Milano, Italy.*

^b *Consorzio Interuniversitario Nazionale per la Scienza e la Tecnologia dei Materiali (INSTM), Via Giusti 9, 50121 Firenze, Italy.*

^c *On leave at: Department of Engineering Physics, Polytechnique Montréal, H3T 1J4 Montreal, Canada.*

* *Corresponding authors: luca.rimoldi@unimi.it; valentina.pifferi@unimi.it; daniela.meroni@unimi.it*

Abstract

One of the key issues of electrochemical sensing in complex matrices is the presence of interferents which can foul the electrode and block the access to the active surface. A possible strategy to promote selectivity is based on the use of interference-abating layers, which can however significantly hamper the sensor response by limiting the analyte diffusion. Here, hard template mesoporous silica films with pore size in the 20-75 nm range and tuneable thickness, deposited onto conductive ITO substrates, were prepared and studied from the physicochemical (FE-SEM, SEM, AFM, water contact angle determinations, UV-vis spectroscopy) and the electrochemical (CV, EIS) point of view. Pore size dependent diffusion phenomena were observed, giving rise to enhanced electrochemical performance for 20-40 nm pores despite the presence of an insulating layer at the electrode surface. The tuneable morphology of the samples together with the wetting properties were found to be pivotal for the understanding of the electrochemical behaviour. The best performance was obtained for the samples with the 20-nm porosity and the highest film thickness. These results were also confirmed by EIS data elaboration, able to provide quantitative measurements about the mass transport resistance of the pores. The modified electrodes were tested for dopamine detection in the presence of a large interfering protein (mucin). The porous and charged network allowed the interfering macromolecule to be excluded, preventing the electrode biofouling and enhancing the performances of the device towards dopamine detection.

Keywords

Porous architecture, hard-templated silica, hydrophilicity, dopamine detection, mucin

1. Introduction

Mesoporous silica-based architectures are attracting a great deal of interest in numerous fields of materials chemistry[1–6]. Templated silicas, either as hollow microparticles[7–9] or porous films[10–13], have recently drawn much attention for sensing and biosensing[14–20], photocatalytic and optical devices[21–23], composites and inorganic-organic hybrids[24–27], drug-delivery and cancer cell detection[28–30], energy conversion and storage systems[31,32], environmental remediation[33–35] and even in positronium generation[36]. In this context, the tuneability of the porous network structure and dimension is of primary importance[1]. For instance, the transport of active species such as analytes, probes, reactants through the oxide network to the catalytic support or the modified electrode surface strictly depends on the dimension and the permeability of the porous structure. In this respect, the traditional approach firstly proposed by Mobil Oil Company[37,38], adopting ionic surfactant liquid crystals as templating agents, provided systems with a rather limited pore range. Anionic or cationic surfactant micelles are able to build well-ordered structures with a pore diameter varying in the range 5–10 nm[39].

In order to create a larger porosity, both non-ionic surfactants and solid templates started to be adopted[40–43]. Polystyrene (PS) monodispersed latex proved to be a useful tool to produce meso- or macro-porous silica with pore dimensions tuneable from about 30 nm to micrometric dimensions. Nonetheless, PS latex has been mostly adopted as template for the preparation of macroporous systems. Kanungo *et al.* focused on the morphological aspects of macroporous silica films by varying experimental parameters and the silica sol composition[44]. Etienne *et al.* studied the electrochemical assisted deposition of hierarchical macro/mesoporous silica films by using 100 nm PS latex and cationic surfactant micelles[45]. The stability of macroporous silica films was investigated by Aluri *et al.*[46], while the possibility to obtain self-supporting membranes was explored by Han *et al.*, once more in the range of macroporosity[47]. All of these studies involved the use of PS latex with a diameter of 0.1–1 μm . On the contrary, the preparation of silica materials with pores larger than those obtained using surfactant micelles, but still in the mesoporosity range, has been scarcely reported in

the literature. The preparation of silica films with pores up to 100 nm would represent a pivotal step towards the development of high-performing electrochemical modified electrodes to be adopted in complex matrices.

In this respect, in recent years, an increased attention has been devoted to the preparation of sensors with antifouling properties[48–50]. Electrode fouling is considered as one of the main issues in the field of sensors, since it prevents the electrode on-line and on-site use due to a decrease of its sensing properties[51,52]. In particular, the analysis of biological matrices greatly suffers from fouling phenomena, due to the complexity of biological fluids and the interferent variety and high concentrations with respect to the analyte[53,54]. In this respect, large proteins and colloidal aggregates (*e.g.* tannin, lecithin, casein micelles) represent widespread interferents which often prevent a reliable determination of trace compounds in real matrices, such as body fluids, food and beverages. Porous architectures with tailored surfaces acting as interference-abating layers are promising in this field, as they improve selectivity by blocking the access of the interferent to the active electrode surface[18,55–59]. Apart from a few notable exceptions[60], these layers, generally with a pore size <10 nm, can significantly hamper the device response by limiting the analyte diffusion.

Here, we report for the first time an engineered electrochemical sensor based on negatively charged mesoporous silica films characterized by a 3D network with much larger pore sizes (up to 75 nm), which proved effective against colloidal interference while preserving good analyte sensitivity. Porous silica films deposited on conductive glass were prepared by adopting PS latex as the templating agent, with a diameter in the 30–100 nm range. The role played by the template dimension and by the number of the deposited layers on the electrochemical and sensing properties was investigated. The modified electrodes were characterized from the morphological, optical and wettability point of view. Electrochemical measurements adopting both negatively- and positively-charged electrochemical probes shed light on diffusion and transport phenomena to the electrode, found to be strictly related to the geometry of the 3D structure. Finally, the present device is

successfully applied for the detection of dopamine, a neurotransmitter whose quantification in biofluids is pivotal for the early diagnosis of the Parkinson's disease, also in the presence of mucin protein as interferent. By a careful tailoring of the pore size, devices with optimal selectivity were prepared while preserving their sensitivity.

2. Experimental section

2.1 Sample preparation

Reactants were purchased from Sigma-Aldrich and adopted without any further purification. Polystyrene (PS) latex suspensions (10% m/v) of three different average diameters (30, 60, and 100 nm) were purchased from Magsphere Inc. (Pasadena, CA, USA). The PS latex beads were not functionalized. The supplier disclosed only the presence of anionic surfactants in the suspension. Indium tin oxide (ITO) covered glass slides (15–25 Ω /sq, Sigma-Aldrich, 2.5 cm \times 2 cm) were used as substrates for film depositions. Solutions were prepared using doubly-distilled water, passed through a Milli-Q apparatus.

ITO-covered supports were cleaned by sonicating in a H₂O/isopropanol (50:50) mixture and in H₂O for 15 min each, then dipped in H₂SO₄ for 30 s (until complete water spreading was observed) to improve silica adhesion, rinsed with water and finally dried under N₂ flux. A silica sol was prepared by a modification of the preparation proposed by Kanungo *et al.*[44]. 16.8 mL of water, 25.4 mL of ethanol, 2.2 mL of HCl 1 M and 4.9 mL of tetraethyl orthosilicate (TEOS) were mixed and stirred for 1 h. The sol was aged for 24 h before use. Right before the deposition, 1 mL of silica sol was mixed with 0.83 mL of a PS latex suspension. Silica films were deposited by spin coating the PS-silica mixture on pre-treated ITO supports (spin time: 30 s, rate: 3000 rpm, ramp: 500 rpm s⁻¹), repeating the procedure for the deposition of multilayers. After drying at room temperature, films were dipped in chloroform for 3 h to remove the PS latex by dissolution, thus creating the sought porosity. Finally, films were rinsed with ethanol and dried at room temperature overnight. At least 3 repetitions of each sample were prepared to verify the reproducibility of the results. No heat treatment was introduced at

the end of the synthesis in order not to affect the 3D porous network of the samples. The as prepared samples are labelled “ $SiO_2_d_n$ ”, where d is the diameter of the adopted PS latex expressed in nanometers, and n is the number of deposited layers. Non-porous films were prepared as reference by adopting the same procedure without the addition of PS spheres. Reference non-porous samples are labelled “ SiO_2_n ”, where n is the number of spin coated layers. A pristine ITO-coated glass was also tested as a reference after washing by sonication in H_2O /isopropanol.

2.2 Materials characterization

Field-Emission Scanning Electron Microscopy (FE-SEM) images were obtained on as prepared films adopting a Zeiss Supra 40 instrument, equipped with a GEMINI column and working in high vacuum. Average pore diameters were determined measuring 160–340 pores for each sample using the ImageJ software. The film thickness was investigated by cross-sectional SEM images (Zeiss EVO50). Atomic Force Microscopy (AFM) images were acquired on a FastScan (Bruker) instrument, working in tapping mode. Root mean squared roughness (RMS) values were determined on $1 \times 1 \mu m^2$ areas. The average dimension of PS latex spheres was measured by Dynamic Light Scattering (DLS, Malvern Zetasizer Nano ZS). The film adhesion was characterized using a TQC model CC3000 apparatus, according to the ISO 2409 standard. UV-vis transmittance spectra were acquired between 250 and 800 nm using a Shimadzu UV2600 spectrophotometer. The contact angle of 5 μL water drops on the silica films was determined using a Krüss EasyDrop instrument. Reported values were obtained averaging at least 5 measurements on different spots, as reported previously[61].

The electrochemical characterization was performed in a three-electrode cell, by using a saturated calomel, a Pt wire and the modified ITO glass as reference, counter and working electrodes, respectively. The geometric electrode area was measured before each analysis for all the samples. In all cases, the geometric surface area always ranged between 1.8 and 2.2 cm^2 . Potassium chloride (Sigma-Aldrich) 0.1 M was used as supporting electrolyte and $[Fe(CN)_6]^{4-}/[Fe(CN)_6]^{3-}$ and $[Ru(NH_3)_6]^{3+}/[Ru(NH_3)_6]^{2+}$ in a concentration of 3 mM as redox probes. Cyclic voltammetry (CV)

and electrochemical impedance spectroscopy (EIS) measurements were performed with a PGstat30 potentiostat/galvanostat (Autolab, The Netherlands), equipped with a FRA module. Each film was analysed over a period of several months and no appreciable changes were observed. The possible occurrence of pre-concentration effects was ruled out by introducing the used electrode in an electrolyte solution without probe. CV analyses were performed scanning the potential in the $-0.3/+0.7$ V (SCE) and in the $+0.2/-0.5$ V (SCE) voltammetric windows in the case of $[\text{Fe}(\text{CN})_6]^{4-}/[\text{Fe}(\text{CN})_6]^{3-}$ and $[\text{Ru}(\text{NH}_3)_6]^{3+}/[\text{Ru}(\text{NH}_3)_6]^{2+}$, respectively. The step potential was fixed at 0.005 V and the scan rate varied between 0.01 and 0.75 V s^{-1} . EIS measurements were carried out at -0.1 , $+0.1$ and $+0.25$ V (SCE) for $[\text{Fe}(\text{CN})_6]^{4-}/[\text{Fe}(\text{CN})_6]^{3-}$ and at $+0.1$, -0.15 and -0.25 V for $[\text{Ru}(\text{NH}_3)_6]^{3+}/[\text{Ru}(\text{NH}_3)_6]^{2+}$. The frequency range was 0.1 – 65000 Hz and the amplitude 0.01 V. The Z-view 3.1 software was adopted for analysis of impedance data.

2.3 Dopamine determination

The electrochemical cell was the same described in the electrochemical characterization paragraph and phosphate buffer 0.1 M pH = 7.4 was used as supporting electrolyte (K_2HPO_4 and NaH_2PO_4). In selected measurements, mucin was added to the electrolyte solution in a concentration of 0.4% w/w. Consecutive additions of 1 mM dopamine were performed to obtain the calibration plots, using differential pulse voltammetry as the electroanalytical technique (Modulation time: 0.05 s; Interval time: 0.5 s; Step Potential: 0.005 V; Modulation Amplitude: 0.05 V). The sensitivity S is represented by the slope of the calibration plot, while LoD and LoQ were calculated by using the following equations: $\text{LoD} = 3.29 s S^{-1}$ and $\text{LoQ} = 10 s S^{-1}$, where s is the standard deviation of the calibration plot.

3. Results and discussion

3.1 Film deposition

Mesoporous SiO₂ films were prepared by spin coating a mixture composed by a hydroalcoholic silica sol containing colloidal SiO₂ nuclei and a hard template suspension (PS latex spheres) on an ITO-coated glass. After drying, the PS spheres embedded into the silica matrix were removed by dissolution in chloroform producing a mesoporous architecture made of interconnected cavities (Fig. 1a). Differently sized PS latex spheres were adopted to tune the morphology of the porous architecture reflecting in differently dimensioned paths to the electroactive support. DLS measurements of the PS latex suspension (Fig. 1b) show a single population with a mean size of 34, 59 and 105 nm for PS beads of 30, 60 and 100 nm nominal diameter, respectively.

All samples exhibited high mechanical stability as proved by ISO 2409 adhesion tests. Samples were firstly crisscrossed with a razor blade forming small squares. Then, an adhesive tape was pressed on the surface of the film and removed applying a constant force under an angle of 60°. Neither appreciable detachment of the SiO₂ layers from the substrate (Fig. S1), nor difference between mono- and multi-layered samples could be appreciated.

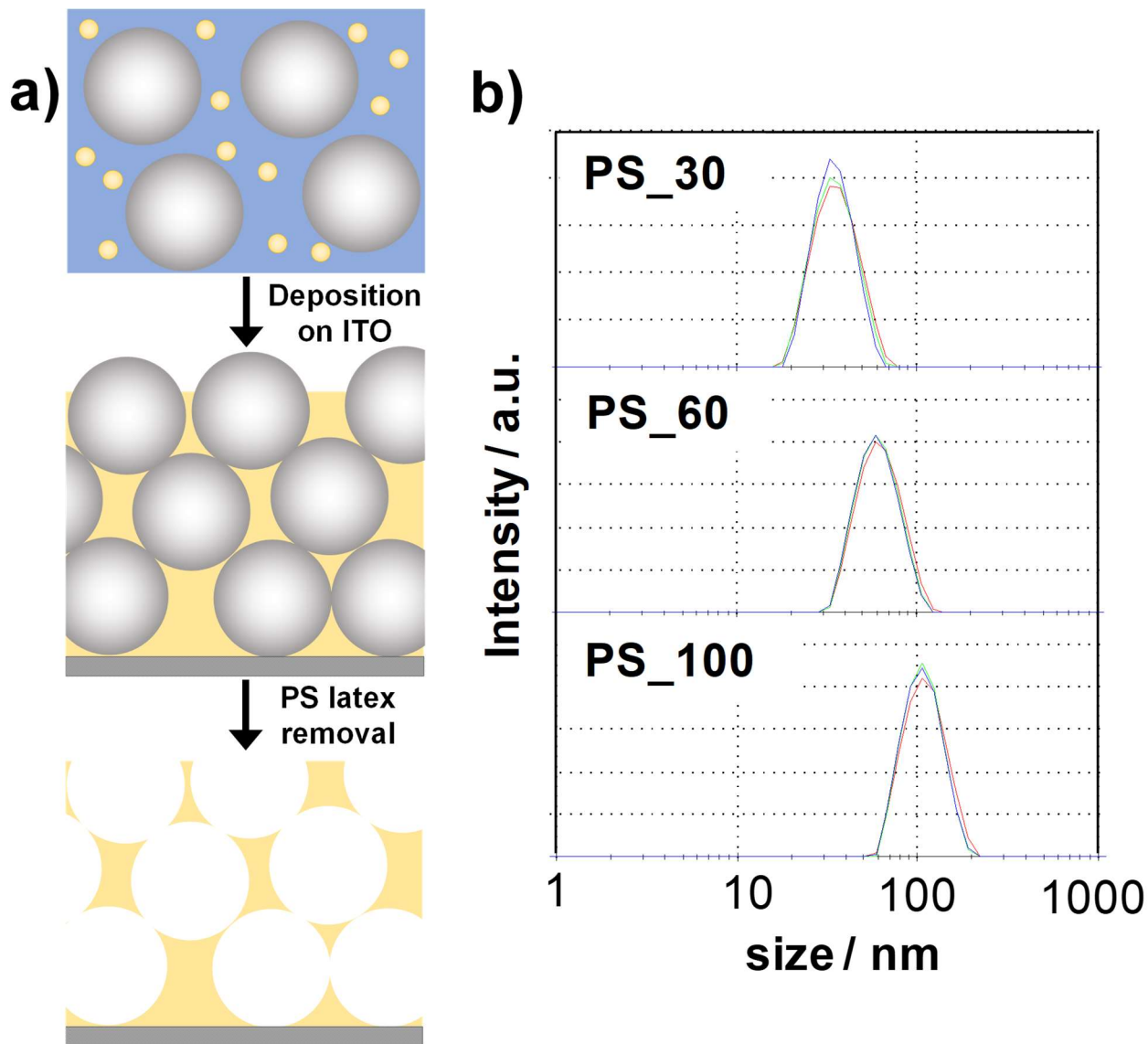


Figure 1 – a) Schematic representation of the mesoporous silica films preparation procedure; small yellow circles and grey circles represent colloidal silica nuclei (actual scale, as reported in ref [62]) and PS latex beads, respectively; b) particle size distribution of the adopted PS latex spheres.

3.2 Morphological properties

The samples morphology was investigated by FE-SEM images (Fig. 2 and S2). Before the template removal, the presence of PS latex spheres embedded in the silica matrix is clearly appreciable (Fig. S2a). Upon template removal, SiO₂_30_n and SiO₂_60_n samples show porosity in the mesopores range (2 – 50 nm, Fig. 2a-b). The homogeneity of the films varies with the PS latex

size: while 30 and 60 nm templates lead to continuous films characterized by a homogeneously distributed porosity and no observable cracking, also in the case of multilayers (Fig. S2b), the 100 nm PS latex resulted in heterogeneous films with macro- and microporous areas (Fig. 2c). The heterogeneity of this sample can be traced back to agglomeration phenomena occurring in the 100 nm PS-SiO₂ sol mixture. The effect of these agglomerates is amplified by the fact that the diameter of the 100 nm PS spheres is comparable to the thickness of a single layer deposition (*vide infra*). The average pore size and pore size distribution also depend on the template size (Fig. 2d): all samples exhibited an average pore size (d_{median} : 22–24 nm, 40–45 nm and 70–75 nm for SiO₂_30_1, SiO₂_60_1 and SiO₂_100_1, respectively) *ca.* 30% smaller than the dimension of the corresponding PS latex spheres used as templates (compare DLS results, Section 3.1). This phenomenon is likely the result of the different embedding degrees of latex spheres within the silica matrix, *i.e.* the nanometric spheres may be completely or only partially embedded into the silica matrix after the deposition. The silica network seems to retain its stability upon removal of the PS latex spheres as appreciable from cross-sectional images showing comparable film thickness before and after template removal (Tab. S1).

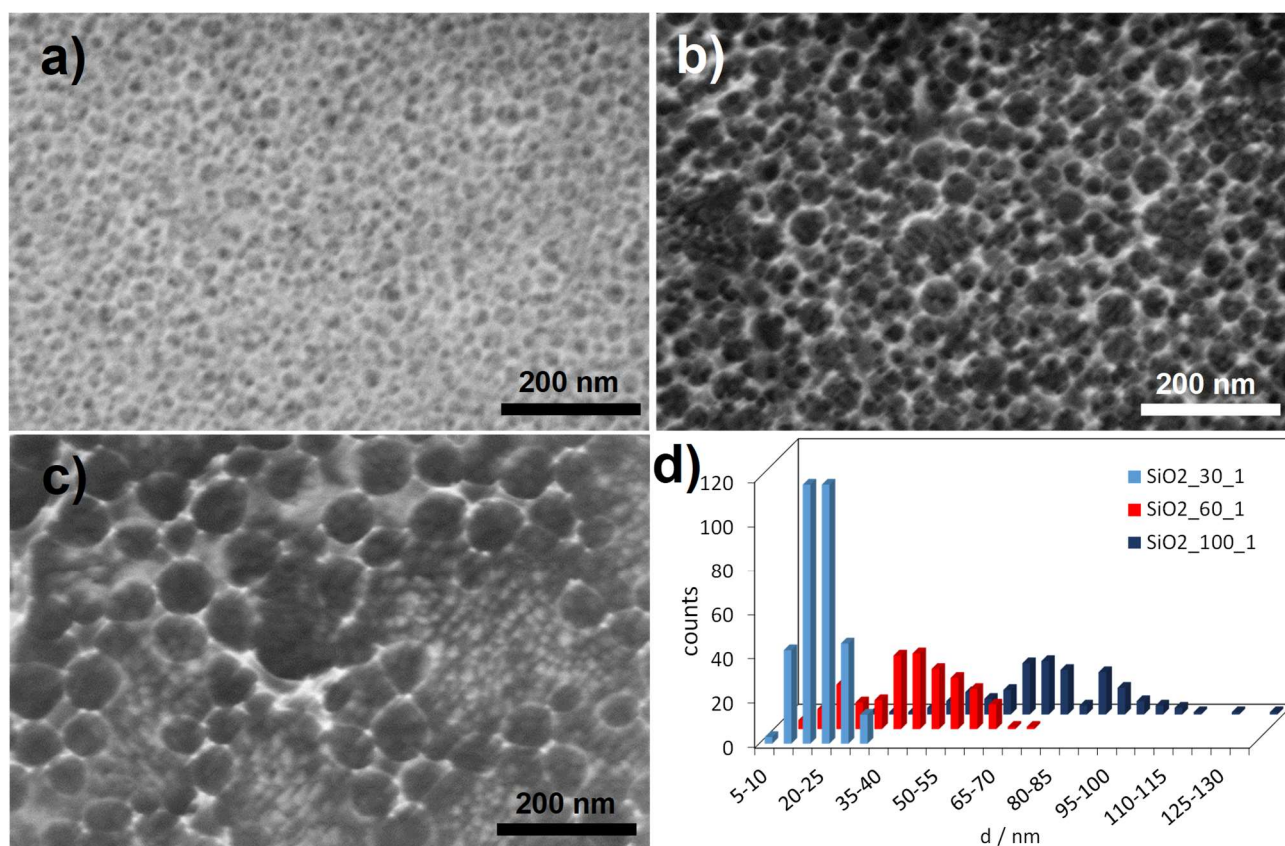


Figure 2 – FE-SEM images of SiO₂_30_1 (a), SiO₂_60_1 (b) and SiO₂_100_1 (c) samples. Pore size distributions as retrieved from FE-SEM images for the different samples (d).

The film morphology was also investigated using AFM measurements (Fig. 3a and S3). AFM images show that the film has nanometric features, that can be related to silica particles. The mesoporosity induced by PS latex spheres is also clearly appreciable, leading to an increase in the sample roughness of about one order of magnitude with respect to the reference samples (RMS: 0.14, 6.3 and 5.6 nm for SiO₂_1, SiO₂_30_1 and SiO₂_60_1, respectively).

The film thickness was determined by cross-sectional SEM images (Fig. 3b and S2) and it was found to be *ca.* 100 nm for each layer, although at increasing the number of layer the thickness becomes more irregular (Fig. S2c). In this context, the dimension of the PS latex adopted was not found to appreciably influence the thickness of the silica films. In high-resolution cross-section micrographs acquired using FE-SEM, the porous network of the samples is clearly appreciable over the whole film thickness (Fig. S2d). It should be noted that the maximum resolution of these

micrographs was limited by the insulating nature of both the sample and the support (in cross section mostly the bare glass is more exposed than the ITO coating).

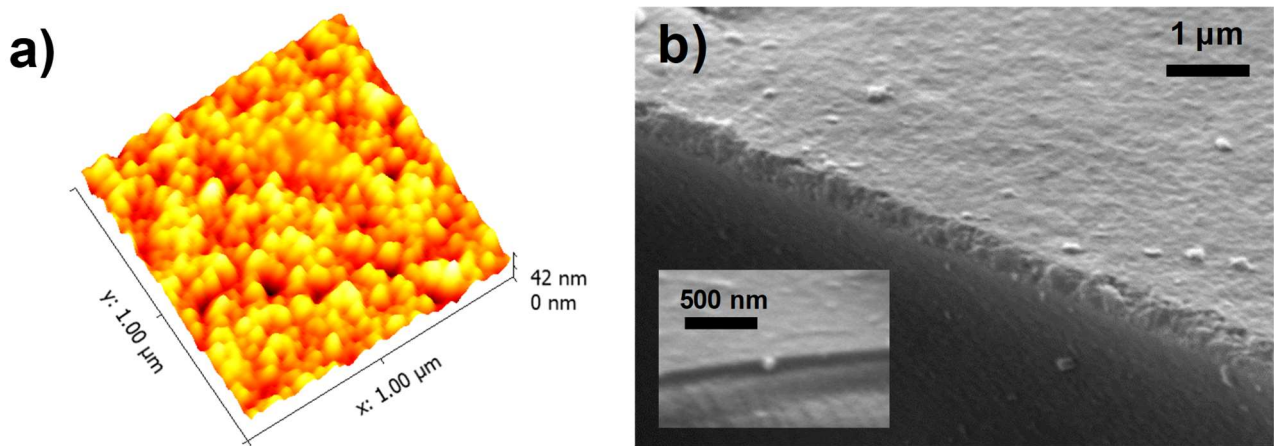


Figure 3 – a) AFM of SiO₂_60_1 and b) cross-sectional SEM images of SiO₂_30_3 and of SiO₂_30_1 (inset). The images were acquired after template removal.

3.3 Optical and wetting properties

The analysis of the optical properties of the samples and of the non-covered substrate show the antireflective properties of the silica films. Similar spectra were obtained for samples synthesized by means of PS latex with a diameter of 30 and 60 nm as an evidence of the samples homogeneity. On the contrary, SiO₂_100_1 sample showed a lower transmittance in the 320–700 nm range, due to macroscopic heterogeneity mirrored in an increased opacity (Fig. 4a). Multi-layered samples did not exhibit significant difference with respect to the corresponding single-layered ones.

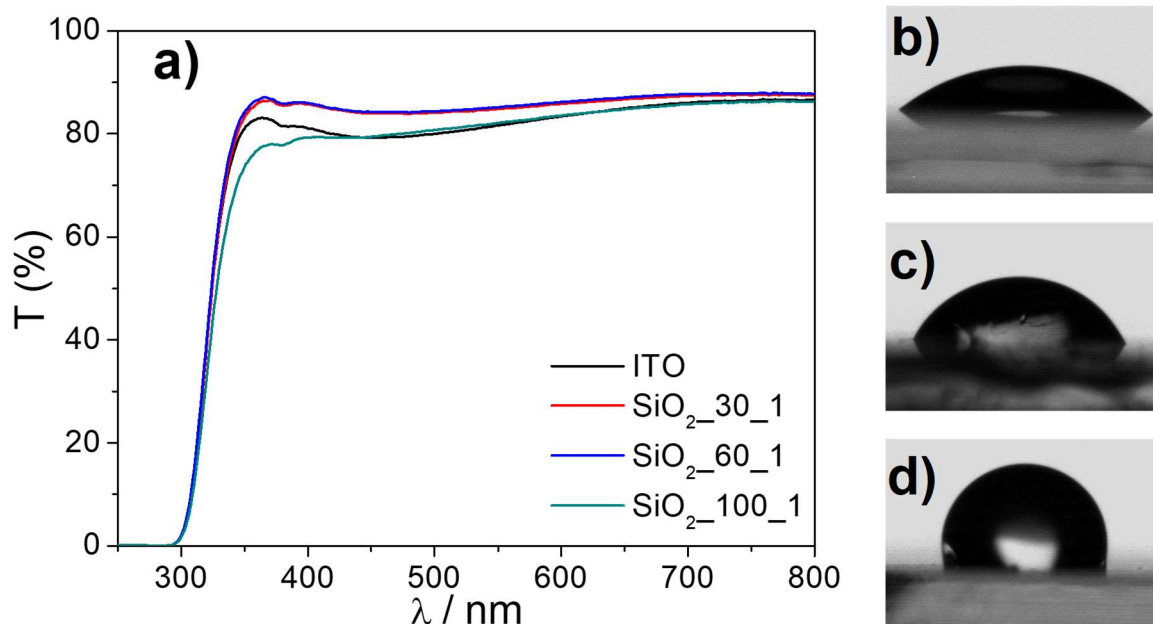


Figure 4 – Transmittance spectra (a) and water contact angles for SiO₂_30_1 (b), SiO₂_60_1 (c) and SiO₂_100_1 (d).

The wetting properties of the silica films were analysed by water contact angle measurements (Fig. 4b-d and Tab. 1). The deposition of a silica layer causes a decrease of the observed water contact angle with respect to bare ITO (θ_w ca. 90° , Fig. S4), as an indication of the higher hydrophilicity of silica with respect to ITO, probably related to a higher surface hydroxylation[63]. Two trends are appreciable: on one hand, increasing the number of layers invariably causes a decrease in water contact angles, more marked in the case of porous films. This behaviour can be explained on the grounds of enhanced water chemisorption resulting from the increased film thickness[64]. Wettability is also affected by the variation of the pore size. Large pores (SiO₂_100_1) show θ_w values comparable to ITO. In this case, both the microscopic and the macroscopic heterogeneity of the film is responsible for the partial exposure of the ITO-coated glass, due to an incomplete substrate coverage, leading to wetting features comparable with those of the bare substrate. More interestingly, smaller pores (SiO₂_30_n) give rise to a higher apparent hydrophilicity than the non-porous silica layer, the more so for increasing number of layers. Intermediate pores (SiO₂_60_n) present wetting

properties more similar to the non-porous silica layer, in the case of the deposition of the first layer, while θ_w values progressively decrease with increasing the number of layers. The superimposition of different layers of not aligned, randomly distributed 60 nm pores yields to a final porosity which resembles that of the smaller pores (see the matching voltammetric results in Section 3.4). In the case of SiO₂_30_n and SiO₂_60_n (with n>1), the observed higher hydrophilicity with respect to the non-porous silica layers can be related to hemiwicking (*i.e.* spreading of a liquid drop on rough hydrophilic surfaces driven by capillarity)[65], arising from the interconnected network of pores[66].

n° layers	water contact angles (°)			
	$d = 0 \text{ nm}$	$d = 30 \text{ nm}$	$d = 60 \text{ nm}$	$d = 100 \text{ nm}$
1	72 ± 5	42 ± 2	73 ± 9	91 ± 9
2	71 ± 4	43 ± 1	62 ± 7	n.a.
3	48 ± 1	36 ± 9	32 ± 3	n.a.
5	41 ± 13	29 ± 5	15 ± 1	n.a.

Table 1 – Water contact angles, in degrees, of silica films as a function of the number of layers and of the size of PS latex spheres, d , used during synthesis (0 stands for the non-porous silica films).

The presence of pores leads to a capillary pull effect, which is stronger in the case of smaller and more hydrophilic pores, as predicted by the Young-Laplace equation[67]:

$$h\rho g = \frac{2\gamma \cos\theta}{r_{pore}} \quad (1)$$

where h is the height of the liquid column in the pore, ρ is the density of the solution, g is the gravitation coefficient, γ is the surface tension of the solution, θ is the contact angle, and r_{pore} is the radius of the pore.

3.4 Voltammetric characterization

Fig. 5a reports the cyclic voltammograms of the SiO₂_d_1 samples, of the reference bare ITO and of the non-porous SiO₂_1 in the presence of the positively charged [Ru(NH₃)₆]³⁺/[Ru(NH₃)₆]²⁺ redox probe. With respect to bare ITO (black continuous line), the non-porous SiO₂_1 sample (black dashed line) shows a drastic decrease of the current response, due to the insulating character of the homogeneous SiO₂ coating[68].

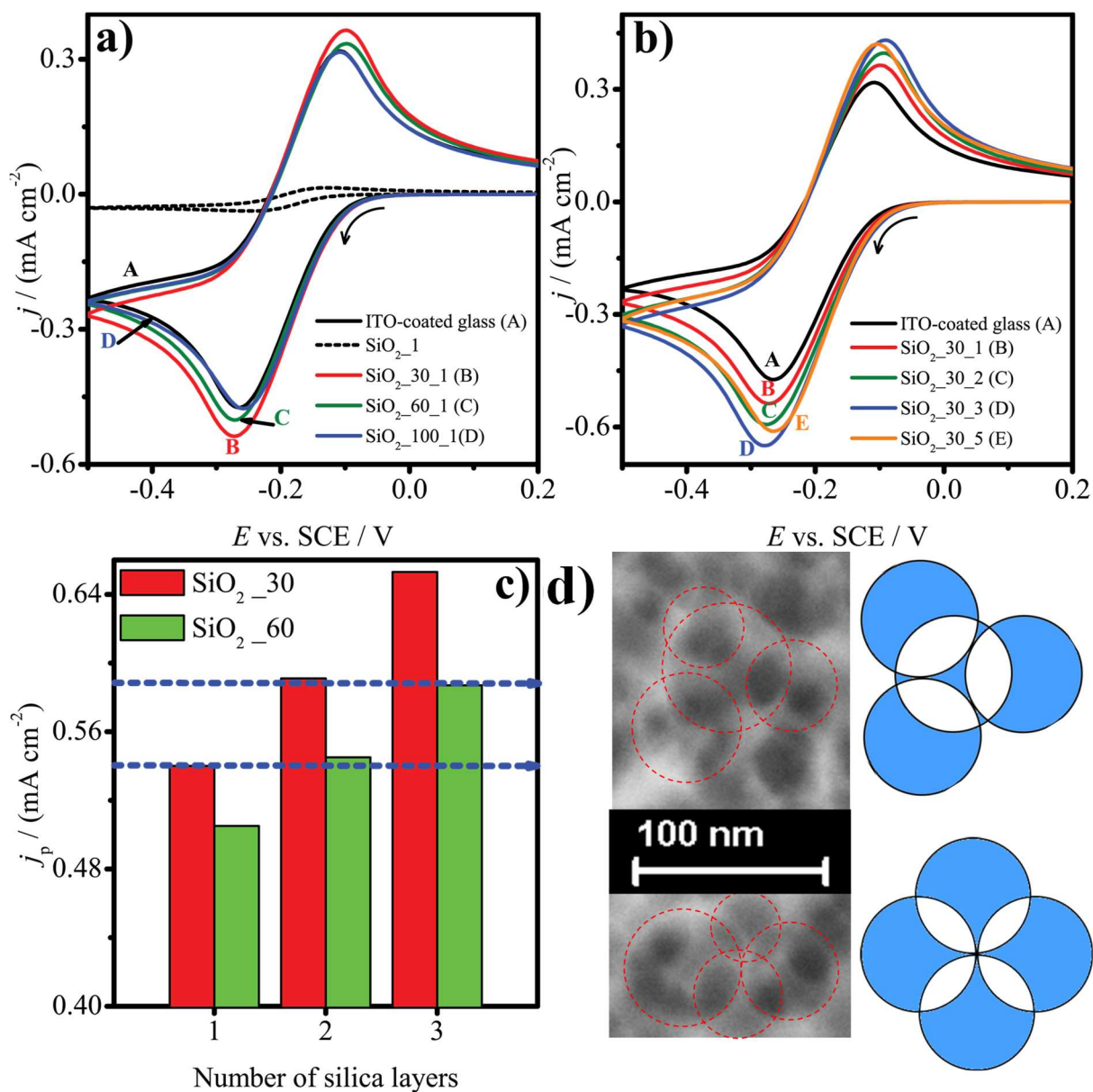


Figure 5 – Cyclic voltammograms of (a) SiO₂_d_1 and (b) SiO₂_30_n samples in the presence of 3 mM [Ru(NH₃)₆]³⁺/[Ru(NH₃)₆]²⁺ probe in 0.1M KCl; scan rate: 100 mV s⁻¹ (c) Comparison of current values for SiO₂_30_n and SiO₂_60_n. (d) SEM image of SiO₂_60_2 sample and scheme illustrating

the shrinking of pore channels (highlighted in blue) resulting from the overlap of different layers of PS spheres.

Mesoporous SiO₂_d_1 samples show peak shaped voltammograms, implying that pores are diffusionally dependent, as expected on the grounds of the lower distance between adjacent pores with respect to their diameters (see SEM results, section 3.2)[69], and that completely convergent diffusion is not present.

Despite the insulating properties of the deposited material, the peak currents of mesoporous structures are comparable (SiO₂_100_1) or even higher (SiO₂_30_1 and SiO₂_60_1) with respect to the bare ITO substrate, with higher values for SiO₂_30_1, due to the presence of smaller pores, which leads to a more intense capillary pull effect (as commented above). The same trends are appreciable in the presence of the negatively charged [Fe(CN)₆]⁴⁻/[Fe(CN)₆]³⁻ redox probe (Fig. S5a): in this case, all peaks of the SiO₂_d_1 samples are an order of magnitude higher with respect to non-porous silica, although remaining lower with respect to the bare ITO peak. The different response of the two probes is due to the attractive or repulsive electrostatic interactions between the two differently charged probes and the silica surface: the deposited oxide (SiO₂) possesses an isoelectric point close to pH 3[70], resulting in a negatively charged surface when immersed in a KCl solution at pH 5–6, whereas in the case of bare ITO the surface can be considered neutral or slightly positive (isoelectric point around pH 6)[71].

Fig. 5b and Fig. S5b report the CV response of SiO₂_30_n samples as a function of the number of deposited silica layers: by increasing the number of layers from 1 to 3, a monotonous growth of the peak current was registered for both probes. By contrast, when five layers of silica are deposited, the peak intensity decreases, since in this case the silica insulating properties probably begin to contrast the favourable effects provided by the mesoporous architecture. Similar results were obtained for the SiO₂_60_n samples (Fig. S6).

The above-reported trends are confirmed by the elaboration of the cyclic voltammetric results by means of the Randles-Sevcik equation (see Table S2 and Fig. S7), whose applicability to the present cases is supported by the values of the slope of $\ln i$ vs. $\ln v$ (Tab. S2, 2nd and 4th column and Fig. S7), which are always close to the theoretical value (0.5)[72] for a diffusive controlled regime. By either decreasing pore size or increasing the number of deposited layers, a progressive increase of the absolute value of the slope of the i_p vs $v^{0.5}$ curve (Tab. S2, 3rd and 5th column) is observed, overcoming the ITO values in the case of the positive probe. Since depositing an insulating layer of mesoporous silica on bare ITO cannot result in an increase of the electroactive area (A), the only parameter which can produce this build-up in the slope value is the increase of the probe diffusion coefficient inside the porous layer (D). Moreover, the increase of the peak to peak separation (Fig. 5a,b) supports a partial loss of electrochemical reversibility of the system in comparison with bare ITO, going from 1 to 3 layers and mainly for the smallest pore diameter (SiO₂_30_n). This phenomenon can also be related to an increase of the mass transport coefficient, thus confirming a growth of the probe diffusion coefficient[72].

The increase of the probe diffusion within the capillaries can be correlated to the analyte concentration enrichment due to the previously cited capillary pull effect. This phenomenon was previously reported in the Literature by other authors on the grounds of experimental evidence[18,19,73].

Apart from the diffusion coefficient change, it should be underlined that a modification of the diffusion mechanism (from fully planar to a mixed planar-radial) has also to be considered due to the presence of shallow pores (*i.e.* pores in which the depth of the pore - nanometers range - is smaller than the size of the diffusion layer - micrometers range)[72]. This morphological characteristic may contribute to the enhancement of the current signal in the presence of porosity.

The comparison among samples with different pore size gives rise to other interesting findings. Fig. 5c shows that the current values reached by SiO₂_60_2 are comparable with those obtained for SiO₂_30_1, while the peak current of the SiO₂_60_3 nearly coincide with that of

SiO₂_30_2 (Fig. 5c), suggesting a decrease of the pore diameter when the number of silica layers is increased. Probably, the random disposition of PS spheres, when successive layers are deposited, produces more tortuous and narrower paths for the electrochemical probe, as can be deduced from Fig. 5d and as supported by wetting data.

3.5 Electrochemical impedance analysis

Fig. 6 shows the EIS trends for SiO₂_30_*n* samples registered at -0.1 V (other potentials give fully comparable results) in the absence of any redox probe. Bare ITO and SiO₂_1 present the same trend, with a straight line covering the entire range of frequencies in the Nyquist plot (Fig. 6a) and phase values very close to 90° for low frequencies (Fig. 6b). In the case of SiO₂_30_*n* samples, the straight line is replaced by a semicircle (Fig. 6a) and phase values at low frequencies deviate from 90° (Fig. 6b), giving rise to a sort of peak in the Bode phase plot. Both phenomena are accentuated increasing the number of silica layers.

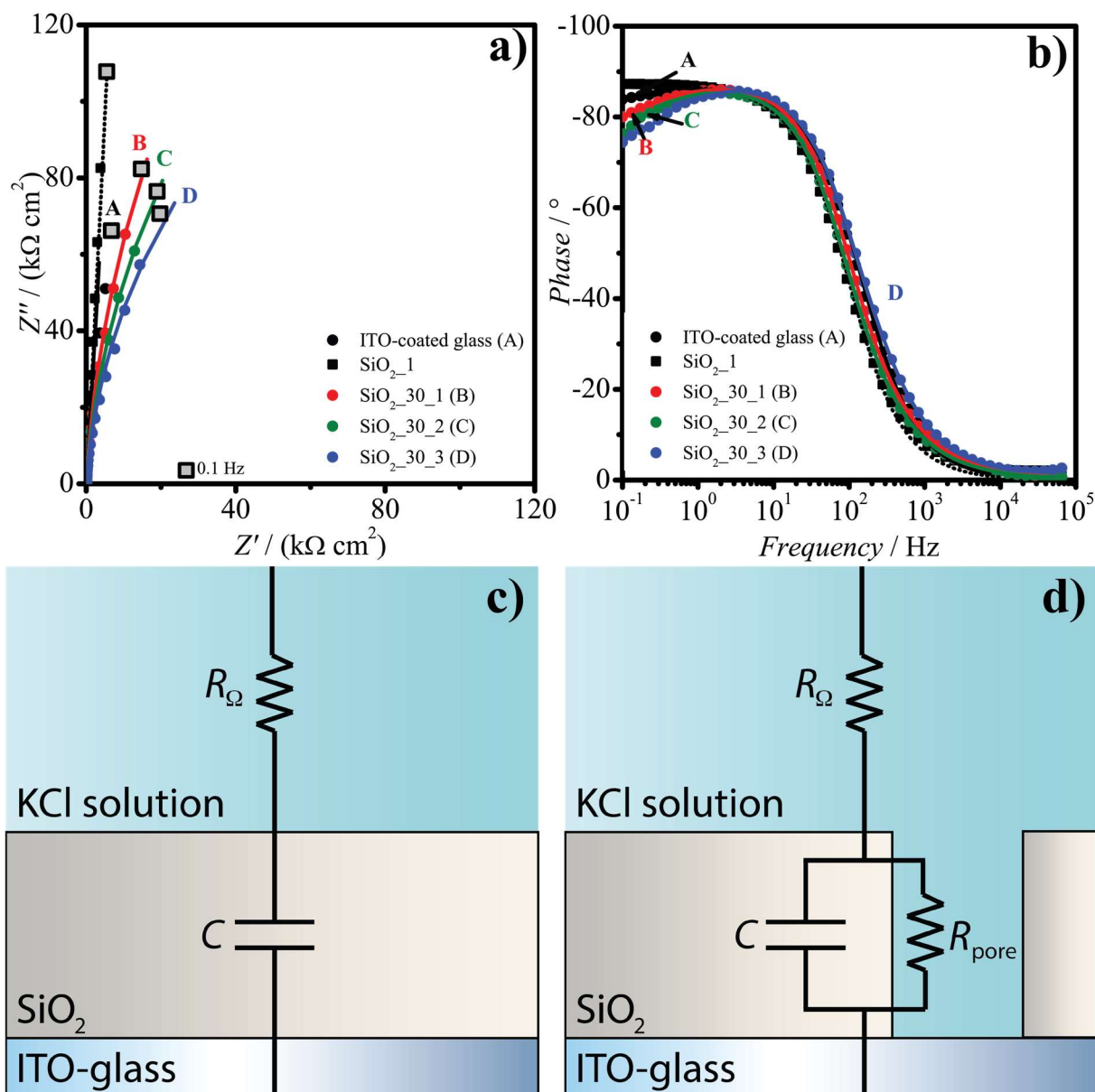


Figure 6 – Complex plane (a) and Bode phase (b) plots for bare ITO support, SiO_2 _1 and SiO_2 _30_n samples registered at -0.1 V in 0.1 M KCl. Equivalent circuits and schematic representation for non-porous silica modified-ITO (and ITO itself) (c) and mesoporous silica modified-ITO (d).

EIS data can be rationalized in terms of two different equivalent circuits (Fig. 6c-d). In the case of the bare ITO support and of non-porous silica samples, the ohmic resistance, R_Ω , is in series with a capacitance C which include the ITO, the double layer and, when present, the silica layer. In other words, these samples behave as pure capacitors. Differently, in the case of mesoporous silica-based samples, an additional resistance R_{pore} in parallel with the capacitance has to be added. Actually,

R_{pore} indicates the resistance of the solution into the pores, which strongly differs from that in the bulk due to the contribute of radial diffusion and to the capillary pull effect previously mentioned.

The resulting EIS parameters are reported in Tab. 2 and S3. R_{Ω} values (Tab. S3, 2nd column) are higher in the case of silica-covered electrodes with respect to bare ITO, more so for non-porous samples, due to the intrinsic insulating character of SiO₂. In general, the capacitances (Tab. S3, 3rd column) are smaller when silica is deposited on the electrodes, since the deposition of an insulating material ideally distances the plates of a capacitor, and when pores are not present the lowest values are reached, since these plates are better spaced. The α values (Tab. S3, 4th column) are very close to 1 for all samples, meaning that the surfaces are macroscopically uniform, also in the case of porous materials[74]. Furthermore, it should be underlined that the smaller the pores, the lower the values of the solution resistance into the pores R_{pore} (Tab. 2) for the same numbers of layers. Moreover, considering equal pore dimensions, the increase of the number of silica layers reflects in lower resistances, confirming the increase of the diffusion coefficient previously discussed.

n° layers	$R_{pore} / (\text{k}\Omega \text{ cm}^2)$		
	$d = 30 \text{ nm}$	$d = 60 \text{ nm}$	$d = 100 \text{ nm}$
1	522	685	1352
2	307	472	n.a.
3	173	399	n.a.

Table 2 – Pore resistance values (R_{pore}) obtained from the fitting of EIS data, registered in 0.1 M KCl, as function of the number of layers and dimension, d , of PS latex spheres.

EIS data registered in the presence of $[\text{Ru}(\text{NH}_3)_6]^{3+}/[\text{Ru}(\text{NH}_3)_6]^{2+}$ (the probe with the best results in cyclic voltammetry thanks also to its positive charge) are not here considered, since the mass transport and the reaction[75] of this molecule are too quick to allow the differences among the electrodes to be appreciated. By contrast, EIS spectra obtained in the presence of $[\text{Fe}(\text{CN})_6]^{4-}/[\text{Fe}(\text{CN})_6]^{3-}$ redox couple (Fig. S8), with a slower mass transport due to the negative charge and a

slower reaction due to the change in the solvation sphere[75], allow to discriminate among the different samples. In the case of ITO, a Randles circuit typical of flat conductive electrodes (Fig. 7a) can be used to fit data: an ohmic resistance R_{Ω} in series with the double layer capacitance C_{dl} , in parallel with the charge transfer resistance R_{ct} and the resistance to the mass transport Z_W , represented with a Warburg element. For the mesoporous electrodes, the circuit (Fig. 7b) is more complicated[74], with the addition of the solution resistance inside the pores R_{pore} , in series with the ITO Randles circuit and the film capacitance C_{film} in parallel. Obviously, the values of R_{ct} ($9.80 \Omega \text{ cm}^2$) and C_{dl} ($0.10 \text{ mF cm}^{-2} \text{ s}^{\alpha-1}$) remain the same than those of ITO (the electrochemical reaction takes place on the surface of ITO also for mesoporous silica electrodes), while values of Z_W can be affected by the modification of the mass transport phenomenon for the presence of the mesoporous layer. Tab. S4 reports the values derived from the EIS fitting.

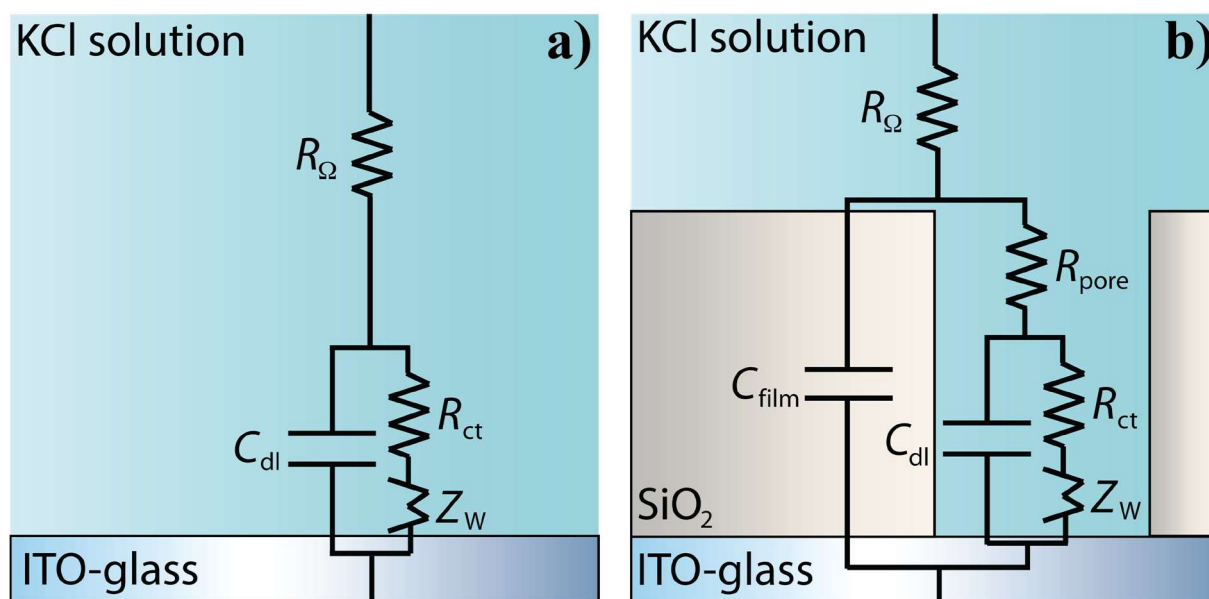


Figure 7 – Equivalent circuits and schematic representation for ITO (a) and mesoporous silica modified-ITO (b) obtained for measurements in the presence of 3 mM $[\text{Fe}(\text{CN})_6]^{4-}/[\text{Fe}(\text{CN})_6]^{3-}$ at + 0.25 V in 0.1 M KCl.

Increasing the pore diameter from 30 to 100 nm and the number of layers, the film capacitance C_{film} decreases depending on the homogeneity and on the thickness of the deposited silica,

respectively. Pore resistance R_{pore} and mass transport resistance Z_{w} values follow a complex behaviour due to a counterbalance of the pull capillary effect and the repulsive electrostatic component brought by the silica layer, confirming the behaviour observed in cyclic voltammetry for the $[\text{Fe}(\text{CN})_6]^{4-}/[\text{Fe}(\text{CN})_6]^{3-}$ probe (Fig. S6b).

3.6 Application in the detection of dopamine

Our samples were tested for the determination of dopamine, an important neurotransmitter widely studied in the field of neurodegenerative diseases, also in the presence of mucin as interferent species. Mucin is a high molecular weight glycoprotein that is a component of mucus and as a result, can be found in a variety of bodily fluids; it is easily adsorbed on electrode surfaces, giving rise to biofouling effects[76,77].

The electroanalytical determination of dopamine in the absence of mucin shows good performances in the case of porous silica electrodes in terms of sensitivity (comparable with that of bare ITO, Fig. 8a) and lower detection limit (Tab. 3). These results are in accordance with what observed in the first part of the manuscript, *i.e.* the promotion of the electrochemical response of the insulating layer due to its tailored porous structure. The electrostatic attractive interactions between the negatively charged silica layers and the monovalent cationic dopamine are presumably less significant than in the case of the multivalent $[\text{Ru}(\text{NH}_3)_6]^{3+}/[\text{Ru}(\text{NH}_3)_6]^{2+}$ probe.

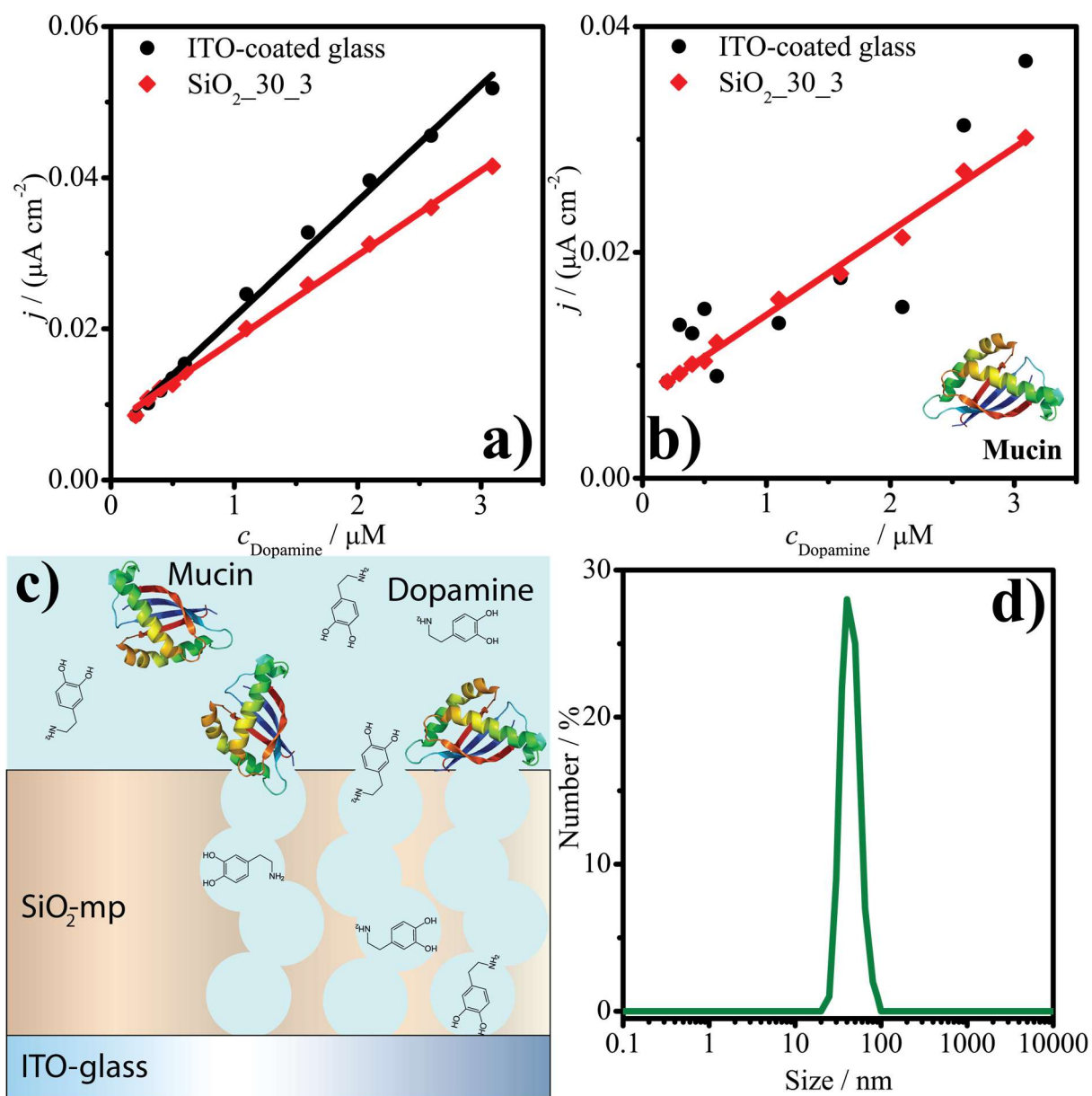


Figure 8 – Calibration plots for dopamine detection in the absence (a) and in the presence (b) of interfering mucin; schematic representation of the selectivity properties in the mesoporous silica detection system (c); DLS of interfering mucin (d).

The porous structure becomes fundamental in the presence of interferents. When interfering mucin is present, the determination of dopamine at low concentration is not possible on bare ITO, since the strong protein adsorption prevents the electron transfer at the electrode surface (Fig. 8b). On the other hand, dopamine is detected in the presence of mucin on $\text{SiO}_2\text{-30}_3$ electrodes (see Fig. S9 for Differential Pulse Voltammetric Scans) and a good calibration plot with slight changes in

sensitivity and detection limits is obtained (Fig. 8b and Tab. 3). The porous structure of silica (with a median pore size of 22-24 nm) allows dopamine (molecule dimension *ca.* 0.8 nm) to reach the active electrode surface underneath the pores (ITO), whilst acting as a barrier for mucin (Fig. 8c) due to both charge repulsion (same charge of silica) and to size exclusion (molecule diameter around 50 nm, as demonstrated by DLS measurements, Fig. 8d).

Sample	$S / (\text{mA cm}^{-2} \text{M}^{-1})$	R^2	LoD / μM	LoQ / μM
ITO	15.3 ± 0.4	0.994	0.271	0.824
SiO₂_30_3	11.2 ± 0.2	0.998	0.156	0.476
ITO + Mucin	-	-	-	-
SiO₂_30_3 + Mucin	7.4 ± 0.2	0.993	0.310	0.944

Table 3 – Analytical parameters obtained from the elaboration of the calibration plot for dopamine in the absence and in the presence of mucin: sensitivity (S), correlation coefficient (R^2), limit of detection (LoD), limit of quantification (LoQ).

4. Conclusions

The tailored structure of mesoporous electrodes can represent the answer to sensor problems arising in real systems. As evidenced by Compton *et al.*[78], the efforts invested in preparing tailored insulating porous layers should be rewarded by the solution of complex problems.

In the present study, the growth of hard-templated mesoporous silica layers onto ITO electrodes has led to comparable or even improved voltammetric responses with respect to the bare electrode, notwithstanding the insulating character of the material. These effects are interpreted as due to the positive combination of tailored morphology, wetting properties and electrostatic effects, resulting in enhanced diffusion/accumulation of the analyte at the electrode surface.

EIS measurements provide an overall framework representing the combination of the different effects, permitting a deep comprehension of the material architecture.

Moreover, the silica mesoporous layer enables a smart control of interfering species during dopamine determination in a complex matrix, permitting its reliable detection. The enhanced selectivity (in terms of the capability of determining particular analyte(s) in a complex mixture without interference from other components in the mixture), which is obtained by the presence of an insulating layer, could have led to a dramatic decrease of the device performance in terms of sensitivities and detection limits. Instead, by tailoring the mesoporous network, an optimal selectivity was achieved while preserving the electrode sensitivity.

The presented approach paves the way to the detection of a wide range of analytes in real matrices, such as body fluids, food and beverages, where interferents such as large proteins and colloidal components often prevent a reliable determination of trace compounds. Its applicability can be further extended by changing the chemical nature of the adopted porous materials. For example, other oxides with different isoelectric points (*e.g.* TiO₂, Al₂O₃) can be selected to promote the exclusion of specific fouling agents.

References

- [1] C. Perego, R. Millini, Porous materials in catalysis: challenges for mesoporous materials, *Chem. Soc. Rev.* 42 (2013) 3956–3976.
- [2] Y. Deng, Y. Cai, Z. Sun, J. Liu, C. Liu, J. Wei, et al., Multifunctional Mesoporous Composite Microspheres with Well-Designed Nanostructure: A Highly Integrated Catalyst System, *J. Am. Chem. Soc.* 132 (2010) 8466–8473.
- [3] A. Walcarius, D. Mandler, J.A. Cox, M. Collinson, O. Lev, Exciting new directions in the intersection of functionalized sol–gel materials with electrochemistry, *J. Mater. Chem.* 15 (2005) 3663.
- [4] A. Vuorema, M. Sillanpää, K.J. Edler, R. Jaber, S.E.C. Dale, S. Bending, et al., Mesoporous Silica Sputter-Coated onto ITO: Electrochemical Processes, Ion Permeability, and Gold Deposition Through NanoPores, *Electroanalysis.* 24 (2012) 1296–1305.

- [5] A. Walcarius, Mesoporous materials and electrochemistry, *Chem. Soc. Rev.* 42 (2013) 4098.
- [6] M. Ogawa, Mesoporous Silica Layer: Preparation and Opportunity, *Chem. Rec.* 17 (2017) 217–232.
- [7] P. Xu, J. Liang, X. Cao, J. Tang, J. Gao, L. Wang, et al., Facile synthesis of monodisperse of hollow mesoporous SiO₂ nanoparticles and in-situ growth of Ag nanoparticles for antibacterial, *J. Colloid Interface Sci.* 474 (2016) 114–118.
- [8] J. Mielby, A.J. Kunov-Kruse, S. Kegnæs, Decomposition of formic acid over silica encapsulated and amine functionalised gold nanoparticles, *J. Catal.* 345 (2017) 149–156.
- [9] W. Li, D. Zhao, Extension of the Stöber Method to Construct Mesoporous SiO₂ and TiO₂ Shells for Uniform Multifunctional Core-Shell Structures, *Adv. Mater.* 25 (2013) 142–149.
- [10] S. Nagarajan, M. Li, R.A. Pai, J.K. Bosworth, P. Busch, D.-M. Smilgies, et al., An Efficient Route to Mesoporous Silica Films with Perpendicular Nanochannels, *Adv. Mater.* 20 (2008) 246–251.
- [11] M.M. Collinson, D.A. Higgins, R. Kommidi, D. Campbell-Rance, Electrodeposited Silicate Films: Importance of Supporting Electrolyte, *Anal. Chem.* 80 (2008) 651–656.
- [12] D. Zhao, P. Yang, N. Melosh, J. Feng, B.F. Chmelka, G.D. Stucky, Continuous Mesoporous Silica Films with Highly Ordered Large Pore Structures, *Adv. Mater.* 10 (1998) 1380–1385.
- [13] M. Kobayashi, K. Susuki, T. Otani, S. Enomoto, H. Otsuji, Y. Kuroda, et al., Thickness control of 3-dimensional mesoporous silica ultrathin films by wet-etching, *Nanoscale.* 9 (2017) 8321–8329.
- [14] A. Walcarius, M.M. Collinson, Analytical Chemistry with Silica Sol-Gels: Traditional Routes to New Materials for Chemical Analysis, *Annu. Rev. Anal. Chem.* 2 (2009) 121–143.
- [15] D. Sun, Y. Zhang, F. Wang, K. Wu, J. Chen, Y. Zhou, Electrochemical sensor for simultaneous detection of ascorbic acid, uric acid and xanthine based on the surface enhancement effect of mesoporous silica, *Sensors Actuators B Chem.* 141 (2009) 641–645.
- [16] M. Saadaoui, I. Fernández, G. Luna, P. Díez, S. Campuzano, N. Raouafi, et al., Label-free

- electrochemical genosensor based on mesoporous silica thin film, *Anal. Bioanal. Chem.* 408 (2016) 7321–7327.
- [17] F. Yan, Y. He, L. Ding, B. Su, Highly Ordered Binary Assembly of Silica Mesochannels and Surfactant Micelles for Extraction and Electrochemical Analysis of Trace Nitroaromatic Explosives and Pesticides, *Anal. Chem.* 87 (2015) 4436–4441.
- [18] T. Nasir, G. Herzog, M. Hébrant, C. Despas, L. Liu, A. Walcarius, Mesoporous Silica Thin Films for Improved Electrochemical Detection of Paraquat, *ACS Sensors.* 3 (2018) 484–493.
- [19] F. Yan, X. Lin, B. Su, Vertically ordered silica mesochannel films: electrochemistry and analytical applications, *Analyst.* 141 (2016) 3482–3495.
- [20] S.Y. Tan, C. Teh, C.Y. Ang, M. Li, P. Li, V. Korzh, et al., Responsive mesoporous silica nanoparticles for sensing of hydrogen peroxide and simultaneous treatment toward heart failure, *Nanoscale.* 9 (2017) 2253–2261.
- [21] Z. Liu, X. Zhang, T. Murakami, A. Fujishima, Sol–gel SiO₂/TiO₂ bilayer films with self-cleaning and antireflection properties, *Sol. Energy Mater. Sol. Cells.* 92 (2008) 1434–1438.
- [22] C. He, B. Tian, J. Zhang, Synthesis of thermally stable and highly ordered bicontinuous cubic mesoporous titania–silica binary oxides with crystalline framework, *Microporous Mesoporous Mater.* 126 (2009) 50–57.
- [23] M. Laskowska, I. Kityk, M. Dulski, J. Jędryka, A. Wojciechowski, J. Jelonekiewicz, et al., Functionalized mesoporous silica thin films as a tunable nonlinear optical material, *Nanoscale.* 9 (2017) 12110–12123.
- [24] M. Faustini, L. Nicole, C. Boissière, P. Innocenzi, C. Sanchez, D. Grosso, Hydrophobic, Antireflective, Self-Cleaning, and Antifogging Sol–Gel Coatings: An Example of Multifunctional Nanostructured Materials for Photovoltaic Cells, *Chem. Mater.* 22 (2010) 4406–4413.
- [25] N. Vilà, A. Walcarius, Electrochemical response of vertically-aligned, ferrocene-functionalized mesoporous silica films: effect of the supporting electrolyte, *Electrochim. Acta.*

179 (2015) 304–314.

- [26] N. Vilà, J. Ghanbaja, E. Aubert, A. Walcarius, Electrochemically Assisted Generation of Highly Ordered Azide-Functionalized Mesoporous Silica for Oriented Hybrid Films, *Angew. Chemie Int. Ed.* 53 (2014) 2945–2950.
- [27] M. Etienne, A. Walcarius, Evaporation induced self-assembly of templated silica and organosilica thin films on various electrode surfaces, *Electrochem. Commun.* 7 (2005) 1449–1456.
- [28] B.-H. Shen, M.-L. Hsieh, H.-Y. Chen, J.-Y. Wu, The preparation of hollow silica spheres with mesoporous shell via polystyrene emulsion latex template and the investigation of ascorbic acid release behavior, *J. Polym. Res.* 20 (2013) 220.
- [29] M.-S. Wu, X.-T. Sun, M.-J. Zhu, H.-Y. Chen, J.-J. Xu, Mesoporous silica film-assisted amplified electrochemiluminescence for cancer cell detection, *Chem. Commun.* 51 (2015) 14072–14075.
- [30] W. Cheng, C. Liang, X. Wang, H. Tsai, G. Liu, Y. Peng, et al., A drug-self-gated and tumor microenvironment-responsive mesoporous silica vehicle: “four-in-one” versatile nanomedicine for targeted multidrug-resistant cancer therapy, *Nanoscale.* 9 (2017) 17063–17073.
- [31] R. Liu, J. Duay, S.B. Lee, Heterogeneous nanostructured electrode materials for electrochemical energy storage, *Chem. Commun.* 47 (2011) 1384–1404.
- [32] Y. Zhang, Z. Zhang, W. Yan, B. Zhang, Y. Feng, A.M. Asiri, et al., Hexagonal mesoporous silica islands to enhance photovoltaic performance of planar junction perovskite solar cells, *J. Mater. Chem. A.* 5 (2017) 1415–1420.
- [33] P. Shinde, S. Sen Gupta, B. Singh, V. Polshettiwar, B.L. V. Prasad, Amphi-functional mesoporous silica nanoparticles for dye separation, *J. Mater. Chem. A.* 5 (2017) 14914–14921.
- [34] M. Okamoto, H. Satake, H. Seki, Base-resistant adsorbents prepared using diamino group-grafted mesoporous silica uniformly coated with zirconia, *J. Mater. Chem. A.* 5 (2017) 24425–

24432.

- [35] K. Fujiwara, Y. Kuwahara, Y. Sumida, H. Yamashita, Synthesis of Ag nanoparticles encapsulated in hollow silica spheres for efficient and selective removal of low-concentrated sulfur compounds, *J. Mater. Chem. A*. 5 (2017) 25431–25437..
- [36] R. Ferragut, S. Aghion, G. Tosi, G. Consolati, F. Quasso, M. Longhi, et al., Positronium Production in Engineered Porous Silica, *J. Phys. Chem. C*. 117 (2013) 26703–26709.
- [37] C.T. Kresge, Ordered mesoporous molecular sieves synthesized by a liquid-crystal template mechanism, *Nature*. 359 (1992) 710–712.
- [38] J.S. Beck, J.C. Vartuli, W.J. Roth, M.E. Leonowicz, C.T. Kresge, K.D. Schmitt, et al., A new family of mesoporous molecular sieves prepared with liquid crystal templates, *J. Am. Chem. Soc.* 114 (1992) 10834–10843.
- [39] Z. Teng, G. Zheng, Y. Dou, W. Li, C. Mou, X. Zhang, et al., Highly Ordered Mesoporous Silica Films with Perpendicular Mesochannels by a Simple Stöber-Solution Growth Approach, *Angew. Chemie Int. Ed.* 51 (2012) 2173–2177.
- [40] P.C.A. Alberius, K.L. Frindell, R.C. Hayward, E.J. Kramer, G.D. Stucky, B.F. Chmelka, General Predictive Syntheses of Cubic, Hexagonal, and Lamellar Silica and Titania Mesostructured Thin Films, *Chem. Mater.* 14 (2002) 3284–3294.
- [41] R. Fan, S. Huh, R. Yan, J. Arnold, P. Yang, Gated proton transport in aligned mesoporous silica films, *Nat. Mater.* 7 (2008) 303–307.
- [42] M. Kanungo, M.M. Collinson, Fabrication of two-dimensionally ordered macroporous silica materials with controllable dimensions, *Chem. Commun.* (2004) 548.
- [43] C. Ma, L. Han, Z. Jiang, Z. Huang, J. Feng, Y. Yao, et al., Growth of Mesoporous Silica Film with Vertical Channels on Substrate Using Gemini Surfactants, *Chem. Mater.* 23 (2011) 3583–3586.
- [44] M. Kanungo, P.N. Deepa, M.M. Collinson, Template-Directed Formation of Hemispherical Cavities of Varying Depth and Diameter in a Silicate Matrix Prepared by the Sol–Gel Process,

Chem. Mater. 16 (2004) 5535–5541

- [45] M. Etienne, S. Sallard, M. Schröder, Y. Guillemin, S. Mascotto, B.M. Smarsly, et al., Electrochemical Generation of Thin Silica Films with Hierarchical Porosity, *Chem. Mater.* 22 (2010) 3426–3432.
- [46] H. Aluri, M.M. Collinson, The stability of nonporous and macroporous titania thin films in aqueous electrolyte solutions, *J. Electroanal. Chem.* 651 (2011) 143–149.
- [47] C. Han, M.-Y. Li, Y. Li, H. Liu, P. Wang, M.M. Collinson, et al., Self-supporting hybrid silica membranes with 3D large-scale ordered interconnected pore architectures, *RSC Adv.* 5 (2015) 19182–19189.
- [48] G. Soliveri, V. Pifferi, G. Panzarasa, S. Ardizzone, G. Cappelletti, D. Meroni, et al., Self-cleaning properties in engineered sensors for dopamine electroanalytical detection, *Analyst.* 140 (2015).
- [49] V. Pifferi, G. Soliveri, G. Panzarasa, S. Ardizzone, G. Cappelletti, D. Meroni, et al., Electrochemical sensors cleaned by light: a proof of concept for on site applications towards integrated monitoring systems, *RSC Adv.* 5 (2015) 71210–71214.
- [50] V. Pifferi, G. Soliveri, G. Panzarasa, G. Cappelletti, D. Meroni, L. Falciola, Photo-renewable electroanalytical sensor for neurotransmitters detection in body fluid mimics, *Anal. Bioanal. Chem.* 408 (2016) 7339–7349.
- [51] C.M.A. Brett, Electrochemical sensors for environmental monitoring. Strategy and examples, *Pure Appl. Chem.* 73 (2001) 1969–1977.
- [52] C.M. Welch, R.G. Compton, The use of nanoparticles in electroanalysis: a review., *Anal. Bioanal. Chem.* 384 (2006) 601–19.
- [53] S. Chandra, A.D. Miller, D.K.Y. Wong, Evaluation of physically small p-phenylacetate-modified carbon electrodes against fouling during dopamine detection in vivo, *Electrochim. Acta.* 101 (2013) 225–231.
- [54] W. Harreither, R. Trouillon, P. Poulin, W. Neri, A.G. Ewing, G. Safina, Cysteine residues

- reduce the severity of dopamine electrochemical fouling, *Electrochim. Acta.* 210 (2016) 622–629.
- [55] Y. Qian, J. Zhu, Y. Li, Single Cylindrical Nanopore Electrodes: Surface Functionalization, Unusual Voltammetry, and Size-Exclusion Properties, *ChemElectroChem.* 5 (2018) 292–299.
- [56] A. Walcarius, E. Sibottier, Electrochemically-induced deposition of amine-functionalized silica films on gold electrodes and application to Cu(II) detection in (hydro)alcoholic medium, *Electroanalysis.* 17 (2005) 1716–1726.
- [57] N. Vilà, E. André, R. Ciganda, J. Ruiz, D. Astruc, A. Walcarius, Molecular Sieving with Vertically Aligned Mesoporous Silica Films and Electronic Wiring through Isolating Nanochannels, *Chem. Mater.* 28 (2016) 2511–2514.
- [58] J. Patel, L. Radhakrishnan, B. Zhao, B. Uppalapati, R.C. Daniels, K.R. Ward, et al., Electrochemical Properties of Nanostructured Porous Gold Electrodes in Biofouling Solutions, *Anal. Chem.* 85 (2013) 11610–11618.
- [59] P. Daggumati, Z. Matharu, L. Wang, E. Seker, Biofouling-Resilient Nanoporous Gold Electrodes for DNA Sensing, *Anal. Chem.* 87 (2015) 8618–8622.
- [60] P. Daggumati, Z. Matharu, E. Seker, Effect of Nanoporous Gold Thin Film Morphology on Electrochemical DNA Sensing, *Anal. Chem.* 87 (2015) 8149–8156.
- [61] G. Soliveri, V. Pifferi, R. Annunziata, L. Rimoldi, V. Aina, G. Cerrato, et al., Alkylsilane–SiO₂ Hybrids. A Concerted Picture of Temperature Effects in Vapor Phase Functionalization, *J. Phys. Chem. C.* 119 (2015) 15390–15400.
- [62] V. Pifferi, L. Rimoldi, D. Meroni, F. Segrado, G. Soliveri, S. Ardizzone, et al., Electrochemical characterization of insulating silica-modified electrodes: Transport properties and physicochemical features, *Electrochem. Commun.* 81 (2017) 102–105.
- [63] J. Drelich, E. Chibowski, D.D. Meng, K. Terpilowski, Hydrophilic and superhydrophilic surfaces and materials, *Soft Matter.* 7 (2011) 9804.
- [64] V.A. Ganesh, a. S. Nair, H.K. Raut, T.M. Walsh, S. Ramakrishna, Photocatalytic

- superhydrophilic TiO₂ coating on glass by electrospinning, *RSC Adv.* 2 (2012) 2067.
- [65] D. Quéré, Wetting and Roughness, *Annu. Rev. Mater. Res.* 38 (2008) 71–99.
- [66] E. Martines, K. Seunarine, H. Morgan, N. Gadegaard, C.D.W. Wilkinson, M.O. Riehle, Superhydrophobicity and Superhydrophilicity of Regular Nanopatterns, *Nano Lett.* 5 (2005) 2097–2103.
- [67] H. Liu, G. Cao, Effectiveness of the Young-Laplace equation at nanoscale, *Sci. Rep.* 6 (2016) 23936.
- [68] V. Pifferi, L. Rimoldi, D. Meroni, F. Segrado, G. Soliveri, S. Ardizzone, et al., Electrochemical characterization of insulating silica-modified electrodes: Transport properties and physicochemical features, *Electrochem. Commun.* 81 (2017) 102–105.
- [69] D. Menshykau, R.G. Compton, Electrodes Modified with Electroinactive Layers: Distinguishing Through-Film Transport from Pinhole (Pore) Diffusion, *Langmuir.* 25 (2009) 2519–2529.
- [70] S. Schwarz, K. Lunkwitz, B. Keßler, U. Spiegler, E. Killmann, W. Jaeger, Adsorption and stability of colloidal silica, *Colloids Surfaces A Physicochem. Eng. Asp.* 163 (2000) 17–27.
- [71] J. Sun, B. V. Velamakanni, W.W. Gerberich, L.F. Francis, Aqueous latex/ceramic nanoparticle dispersions: colloidal stability and coating properties, *J. Colloid Interface Sci.* 280 (2004) 387–399.
- [72] R.G. Compton, C.E. Banks, *Understanding Voltammetry*, 2nd ed., Imperial College Press, Oxford, 2007.
- [73] F.G. Chevallier, L. Jiang, T.G.J. Jones, R.G. Compton, Mathematical modelling and numerical simulation of cyclic voltammetry at an electrode covered with an insulating film containing cylindrical micropores, *J. Electroanal. Chem.* 587 (2006) 254–262.
- [74] M.E. Orazem, B. Tribollet, *Electrochemical Impedance Spectroscopy*, John Wiley & Sons, Inc., Hoboken, NJ, USA, 2008.
- [75] T. Doneux, A. de Ghellinck, E. Triffaux, N. Brouette, M. Sferrazza, C. Buess-Herman,

Electron Transfer Across an Antifouling Mercapto-hepta(ethylene glycol) Self-Assembled Monolayer, *J. Phys. Chem. C.* 120 (2016) 15915–15922.

- [76] G. Di Carlo, A. Trani, D. Zane, G.M. Ingo, M. Pasquali, A. Dell’Era, et al., Influence of Different Biological Environments on Serotonin (5-HT) Electrochemical Behavior at Gold Screen Printed Electrodes, *Electroanalysis.* 26 (2014) 1409–1418.
- [77] A. Fagan-Murphy, F. Watt, K.A. Morgan, B.A. Patel, Influence of different biological environments on the stability of serotonin detection on carbon-based electrodes, *J. Electroanal. Chem.* 684 (2012) 1–5.
- [78] H.T.H. Chan, E. Kätelhön, R.G. Compton, Voltammetry at electrodes decorated with an insulating porous film: Understanding the effects of adsorption, *J. Electroanal. Chem.* 801 (2017) 135–140.